AIAA JOURNAL
Vol. 48, No. 10, October 2010

High-Resolution Simulations of Parallel Blade–Vortex Interactions

Alasdair Thom*
University of Glasgow, Glasgow G12 8QQ, United Kingdom
and
Karthikeyan Duraisamy†
Stanford University, Stanford, California 94305

DOI: 10.2514/1.J050381

The physics of a parallel blade–vortex interaction is studied numerically and the predicted pressure and acoustic results are compared with experimental measurements. A high-resolution solution of the compressible Euler equations is performed on structured overset meshes. Initially, a two-dimensional airfoil–vortex interaction is studied for both a case where the vortex misses the blade and a case of direct impact. The vortex is initiated in the flow as a perturbation to the freestream conditions and is free to evolve, thus allowing for the deformation of the vortex as it interacts with the blade to be studied. The simulation is seen to accurately reproduce the experimental results and the emission of the acoustic waves from the airfoil surface is observed in detail. Acoustic energy generated by the interaction is seen to primarily radiate from the leading-edge section of the airfoil with a weaker contribution coming from the trailing edge. The simulations are then extended to three-dimensional moving overset meshes where the vortex generation and convection is also resolved. The numerical methodology is seen to accurately preserve the vortex strength and accurately reproduce the experimentally measured blade surface pressures and acoustics. The computations presented here face similar challenges to that encountered in the simulation of realistic helicopter blade–vortex interaction, but the computational costs are such that the solutions can be well resolved, and comprehensively validated using moderate resources.

Nomenclature

C_p	=	perturbation pressure coefficient, $(p - p_s)/\frac{1}{2}\rho_\infty U_\infty^2$
c	=	rotor blade chord
p	=	instantaneous airfoil surface pressure
p_s	=	steady airfoil surface pressure
R	=	rotor radius
r_c	=	vortex core
r	=	distance from vortex core
strong BVI	=	strong interaction, $\frac{Z_v}{c} = 0.0$
U_∞	=	freestream velocity
V_θ	=	vortex swirl velocity
weak BVI	=	weak interaction, $\frac{Z_v}{c} = 0.25$
Z_v	=	vortex/blade miss distance (chords)
Γ	=	vortex circulation
ψ	=	rotor azimuth
ψ_{eqv}	=	equivalent rotor azimuth, used to interpret two-dimensional airfoil–vortex interaction computations

Introduction

A MAJOR source of rotorcraft noise is generated by the rotor blades interacting with the vortices trailed from the preceding blades. This blade–vortex interaction (BVI) generates high amplitude impulsive noise that is particularly intense under certain flight conditions such as low speed descent and manoeuvre, where the proximity of the trailed vortices induces rapid changes in loads on the rotor blades. BVI noise is especially important because it is known to propagate out-of-plane of the rotor and towards the ground [1], and is in a frequency range to which the human ear is highly receptive. Therefore, there exists great interest in studying BVI noise and vibration, with the motivation arising from ever more stringent noise requirements.

The capability to accurately predict the aerodynamics and acoustics of BVIs on a helicopter rotor would be of great use to helicopter designers, and over the past few decades BVI has been the focus of much experimental, theoretical and computational research. A recent example of an experimental study involving model rotor configurations is the higher harmonic control aeroacoustics rotor tests [2,3]. These tests were performed on a Mach-scaled Bo-105 rotor and the blade loads, wake velocities and noise were measured over a range of descending flight conditions. Despite the complexities of a full rotor, much work has gone into simulating such a case. A prime example is the work of Lim et al. [4], in which a grid of 108 million points was used to resolve the flow over a helicopter rotor in descending flight using a Reynolds-averaged Navier–Stokes (RANS) solver coupled to a structural dynamics code. Though the agreement of the computed airloads and acoustics with experimental measurements is encouraging and proved to be an improvement compared with that from low order models, several discrepancies still exist, a significant proportion of which is attributed to numerical dissipation error arising from the use of coarse meshes. For instance, the mesh size in the finest region of the wake was 5% of the blade chord, whereas previous work [5,6] has indicated that the resolution needs to be at least 5 times finer in each coordinate direction. Even with recent advances in high performance computing, such a well resolved computation appears to be out of reach, at least in the forthcoming future. To develop confidence in simulations over such a realistic flowfield, it must first be ensured that the relevant flow physics is sufficiently well modeled in a representative, but simpler flow. Therefore, the need to make detailed and comprehensive evaluations of the flow solver on simpler flow configurations is paramount. It is equally important to pursue such evaluations in a generic framework that can be easily extended to three-dimensional realistic configurations.

Received 7 December 2009; revision received 2 March 2010; accepted for publication 22 April 2010.

*Postgraduate Research Student, Department of Aerospace Engineering; athom@eng.gla.ac.uk.

†Consulting Assistant Professor, Department of Aeronautics and Astronautics; dkarthik@stanford.edu.

The experimental work of near-parallel BVI carried out by Caradonna and Kitaplioglu [7] studied the fundamentals of a BVI in a simplified configuration. In this work, an independent free vortex approach is employed, where the vortex is generated by a fixed wing placed upstream of the rotor. The vortex convects downstream to the rotor which is operated at zero thrust to minimize the generation of its own vortices. The rotor was also stiffened to minimize blade flapping. This approach retains the key features of a BVI while significantly reducing the complexity of the problem, allowing parameters such as the vortex position and strength to be studied. The simplicity of this experiment makes it ideal for a fundamental study of BVI and for validating the computational prediction of blade pressures and acoustics. Similar experimental work has been performed by Horner et al. [8] involving parallel and perpendicular interactions where the vortices are generated by split wings.

At the simplest level, a parallel BVI problem can be reduced to a two-dimensional airfoil–vortex interaction (AVI). This approach is ideal to study the underlying physical mechanisms involved in the interaction as it removes many of the complications of a three-dimensional BVI simulation and is computationally less expensive. One of the major challenges faced when simulating an AVI is to preserve the vortex structure accurately as it convects through the solution and minimize the numerical dissipation that is inherent in computational fluid dynamics (CFD) simulations. The work of Oh et al. [9] addressed this problem by the use of adaptive unstructured meshes to simulate a two-dimensional AVI. This method dynamically concentrates mesh points in region of large flow gradients, providing high resolution in the region of any vortices and other important flow features. Excellent results were achieved in this study but this method can be complex to implement, especially if extended to realistic rotor configurations.

The work of Morvant et al. [10] used a compressible vorticity confinement method to preserve the vortices and was able to achieve good results on relatively coarse meshes. However, vorticity confinement is not a mature technology, especially because it requires the specification of empirical confinement parameters. There has also been promising work studying the viscous effects present during an AVI, the work of Ilie [11] is a prime example. Here the effects of separation present during the interaction were captured using a large eddy simulation (LES) approach. However the computational cost associated with LES make this approach unfeasible for realistic rotor configurations in the foreseeable future.

In the present work, two-dimensional AVI simulations are preformed using high-resolution techniques to preserve the vortex. The pressure and acoustic results are compared with the experiments of Caradonna and Kitaplioglu [7] of a near-parallel BVI. An attempt is then made to simulate the experiments of Caradonna and Kitaplioglu [7] in three dimensions. To do this the method of moving overset meshes is utilized. Much work has go into studying this experiment in the past, from indicial models [12], to potential models [13], to full CFD Euler/Navier–Stokes models [14–16]. Although the lower order models capture the basic trends, the CFD methods naturally capture more detail, but did not offer significantly improved predictions. In the CFD approaches the vortex was imposed in the solution as a constant strength perturbation using a vortex fitting method. This method has produced accurate results for a weak interaction case, where the vortex passes below the blade, but is unable to accurately capture a case of strong interaction where the vortex impact directly on the blade [17].

The novelty of the present work arises from the fact that an attempt is made at fully resolving (in three dimensions) the vortex generation, convection and interaction. The computations are thus faced with challenges similar to that encountered in the simulation of realistic flight conditions of a helicopter, but the computational costs are such that the solutions can be well resolved using moderate resources.

Computational Methodology

The compressible hybrid RANS/LES solver CHRONoS [18] is used for the simulations. The methodology uses a vertex-centered finite volume solution on structured overset meshes. The use of overset meshes allows for a high degree of flexibility in generating high quality meshes and to efficiently distribute mesh points in the vortex dominated regions of the flow. To more clearly identify numerical diffusion errors, the present simulations are restricted to the solution of the Euler equations. For the spatial differencing, fifth order accurate upwind differencing is utilized [19], while the second order implicit backward differencing scheme is used for time integration. Dual time stepping [20] (with a constant pseudo-Courant–Friedrichs–Lewy number) is used to minimize factorization and linearization errors. Linear acoustic analysis is performed using the Farassat-1A on-surface formulation [21] of the Ffowcs–Williams and Hawking equations. This formulation accounts for the monopole and dipole sources of noise and has been shown to accurately predict helicopter acoustics [22]. In this analysis, the rotor blade surface pressure obtained from the CFD solution are used to calculate the near-field and far-field acoustic pressures, accounting for both monopole and dipole sources of noise from the blade. Quadrupole noise sources which are due to fluid stress are neglected. These sources have been shown to be negligible for this interaction [23].

Table 1 Conditions of experiments

	M_{tip}	M_∞	Z_v	μ
Weak interaction	0.715	0.142	0.25	0.198
Strong interaction	0.715	0.142	0.0	0.198

AVI

The dominant features of a near-parallel BVI are quasi-two-dimensional, and the surface pressure pulse produced from this BVI can be simulated using an idealized two-dimensional AVI simulation. A high-resolution AVI simulation is significantly less expensive than a three-dimensional BVI simulation. The value of such a simulation is that much of the fundamental flow physics of a three-dimensional parallel BVI are present in the two-dimensional case, but can be studied in a much simpler context. It is also more feasible to keep numerical diffusion errors to a minimum in a two-dimensional AVI simulation and the calculations can offer a clear indication of the mesh requirements to resolve the interactions to sufficient detail in a full simulation.

The parallel BVI experiments of Caradonna et al. [24] are an ideal reference for the present study because of two-dimensional nature of the experiment. This study involved a nonlifting rotor interacting with a vortex independently generated upstream. The rotor blade was untwisted and stiffened to minimize vibration with NACA 0012 airfoil and a rectangular planform. The vortex generator had a NACA 0015 section and its incidence and position was altered to change to vortex strength and vortex/rotor miss distance of the experiment. Chordwise surface pressure measurements were obtained at various

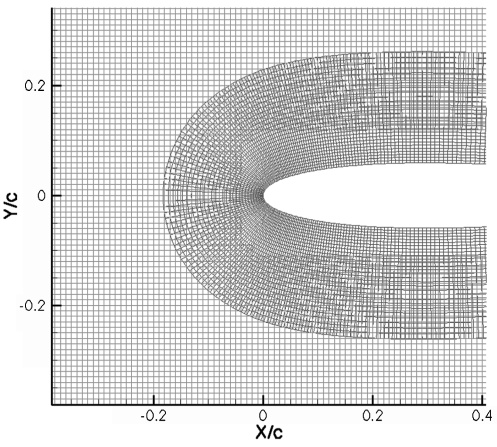

Fig. 1 Detail of high-resolution AVI blade and Cartesian mesh.

Table 2 Number of cells in AVI meshes

	Blade	Cartesian	Total points
High resolution	425×30	901×261	247,991
Low resolution	261×73	325×156	37,253

radial locations and acoustic data was also measured in the near field (approximately three chords from the interaction) of the interaction and the far field (approximately 20 chords from the interaction). The experiments involved various BVI configurations, however, the conditions used in the present simulations are summarized in Table 1. As this experiment involved a near-parallel BVI, the interaction can be approximated as a quasi-two-dimensional AVI.

The AVI analysis is performed on a two mesh system; a body-conforming C topology mesh to discretize the near-blade domain of a NACA 0012 airfoil, which is overset onto a larger Cartesian mesh. A detail of the AVI mesh can be seen in Fig. 1. To verify grid convergence the simulations are performed on both a high and a low-resolution mesh system and the mesh dimensions are summarized in Table 2. The high-resolution Cartesian mesh has a grid spacing of $0.01c$ in the region where the vortex convects, guaranteeing approximately 32 points across the vortex core throughout the simulation. The high-resolution blade mesh has a compact design where its outer boundary is approximately a distance of $0.2c$ from the airfoil surface. The spacing at the leading edge on the airfoil surface is $0.001c$ and the spacing at its outer boundary is similar to the surrounding Cartesian mesh to promote accurate data interpolation between the meshes. This resolution has been shown to be more than sufficient at preserving idealized vortices with a 5th order accurate numerical scheme [6,25].

The low-resolution Cartesian mesh has a grid spacing of $0.035c$ in region where the vortex convects, producing approximately eight points across the vortex core throughout the simulation. The blade mesh has an outer boundary a distance of $0.8c$ from the airfoil surface. Mesh spacing at the leading edge of the airfoil surface is $0.002c$ and $0.035c$ at the blade mesh boundary to match the surrounding Cartesian mesh and promote accurate data interpolation. These dimensions were chosen to closely match the mesh dimensions of the succeeding three-dimensional BVI simulations.

The simulation is first run until a steady solution has been achieved for the nonlifting airfoil. The freestream Mach number is 0.626 which corresponds to the velocity normal to the rotor blade at 87% radius of the rotor at the point of interaction in the experimental study. This location was chosen as it is in the tip region of the rotor and also because of the availability of experimental pressure measurements. The three-dimensional effect due to the tangential velocity component is not accounted for in the two-dimensional AVI simulations. Once a steady value is reached the swirl velocity profile of the vortex is prescribed upstream of the airfoil as a perturbation[‡] to the steady flowfield:

$$V_\theta(r) = \frac{\Gamma}{2\pi} \frac{r}{(r_c^2 + r^2)} \tag{1}$$

With values of vortex circulation and core radius of $\Gamma = 1.122 U_\infty c$ and $r_c = 0.162c$, respectively, where c is the rotor chord length. These parameters are obtained from the experimental work of McAlister and Takahashi [26] where the vortex trailed from a NACA 0015 wing was studied. The approach of using the McAlister vortex data to simulate the Caradonna experiments has been widely used before in similar simulations [23], however, most previous studies have imposed the vortex as a moving, constant strength perturbation from the field velocity [23]. In the present work, the vortex is free to convect and deform, allowing a strong interaction case where the vortex directly impacts upon the blade to be realistically simulated. The vortex was initiated two chords ahead of the airfoil, and the simulation is advanced with time steps of 0.0025 and 10 subiterations per time step. The results were found to be independent of the vortex initiation location at distances above approximately 1.5 chords ahead of the airfoil.

To accurately simulate the AVI, the strength of the vortex must be preserved as it convects through the Cartesian mesh. Figure 2 shows the vortex velocity profile as the vortex convects through both the high and low-resolution Cartesian meshes. No significant decay of the vortex is seen in either cases and the numerical scheme is found to sufficiently preserve the vortex structure.

AVI Surface Pressure Results

The simulation is first performed on a case where the vortex passes below the blade with a miss distance of a quarter chord ($Z_v = 0.25c$), which will be referred to as a weak interaction. This case was chosen to serve as a verification as similar cases have previously been simulated successfully [23]. The perturbation pressure coefficient is shown in Fig. 3a for the lower surface of the airfoil at a chordwise location of $x/c = 0.02$. This point on the airfoil surface is the closest to the leading edge of the experimental measurement set, and is subject to the sharpest pressure gradients. Note that the solution time of the two-dimensional simulation has been converted to the equivalent of rotor azimuth to directly compare against experiment. Also the pressure value has been offset to best correspond with the experimental data. This is done as the experimental data was averaged to have a mean value of zero for a full rotor revolution, meaning the absolute pressure value at any point is arbitrary but the relative change of pressure is accurate. An abrupt pressure pulse is observed during the interaction and is the most prominent feature of the AVI event. The computed pressure pulse agrees well with the experimental results in both phase and magnitude in spite of this being a two-dimensional simulation. This highlights the highly two-dimensional nature of the interaction and similar results have been obtained in previous work [27]. At the later azimuths (beyond 200°), the computed pressures begin to diverge from the experimental data due to the blade becoming more oblique to the vortex in the experiment.

A strong interaction case of zero miss distance ($\frac{Z_v}{c} = 0.0$) where the vortex impacts directly upon the blade is a more challenging case to simulate due to the expected deformation of the vortex. It has been previously shown [28] that this deformation of the vortex must be accurately captured if the surface pressures on the blade are to be correctly predicted. The computed pressure response of a strong AVI is shown in Fig. 3b and compared with the experimental data. Again, the results agree well in magnitude and phase, suggesting that the relevant physics and vortex deformation is accurately represented in both the high- and low-resolution cases. The pressure pulse generated by the strong interaction has a similar shape to the weak interaction case but is greater in magnitude. The CFD results and the experimental data differ in phase but it should be noted that in the experimental setup there was an uncertainty as to the exact location of

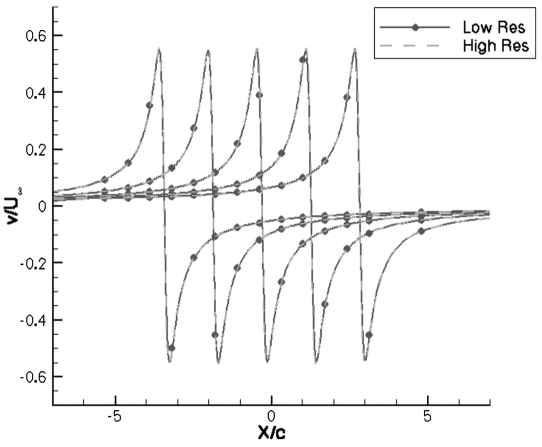

Fig. 2 Vortex velocity profile as vortex convects in positive x direction.

[‡]The density and pressure perturbations are determined using the tangential momentum equation and constant enthalpy conditions.

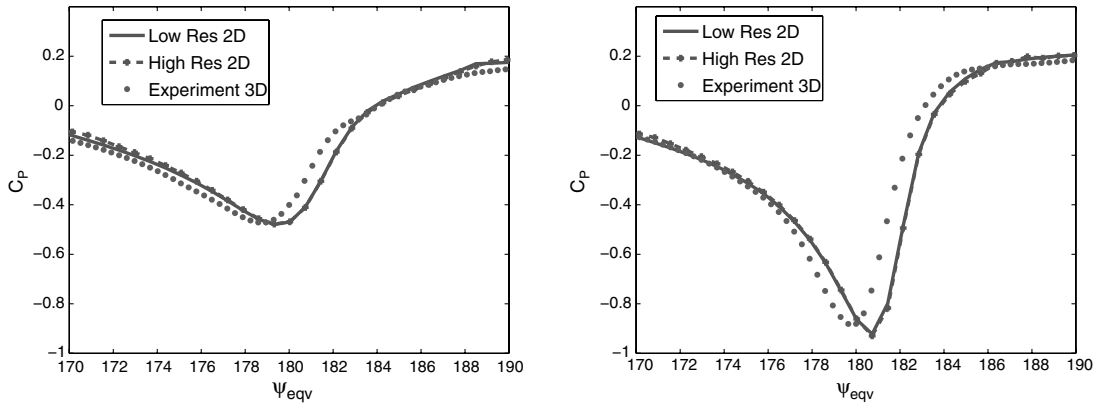

a) Weak AVI **b) Strong AVI**

Fig. 3 Perturbation pressure at $x/c = 0.02$ on the lower surface of the airfoil for weak and strong AVI. Both the low and high-resolution meshes are shown.

the vortex position [24]. Differences between the three-dimensional experimental data and the computed two-dimensional CFD results most likely arise from the unsteady velocity experienced by the experimental rotor blade. The two-dimensional simulations did not account for this and a steady freestream velocity was prescribed in all simulation. It was verified, however, that the unsteady velocity effects present on the three-dimensional blade caused minimal pressure changes.

The experimental and computed (high-resolution) perturbation pressures over the entire surface of the airfoil are shown in Figs. 4 and 5 for the weak and the strong interaction cases, respectively. Kitaplioglu et al. [29] noted that the interaction involves two distinct waves. The primary wave is initiated at the leading edge and causes a pressure wave to travel rapidly along the chord from the leading to the trailing edge. This pressure wave begins with the pulse shown in Fig. 3a and has its greatest magnitude at the leading edge. This is followed by a relatively stable period of constant pressure on the airfoil surface. Once the vortex passes the trailing edge, the reestablishment of the Kutta condition causes a secondary, weaker wave to travel upstream from the trailing to the leading edge. These two events create a distinct triangular structure on the surface pressures and have been captured in the two-dimensional simulations.

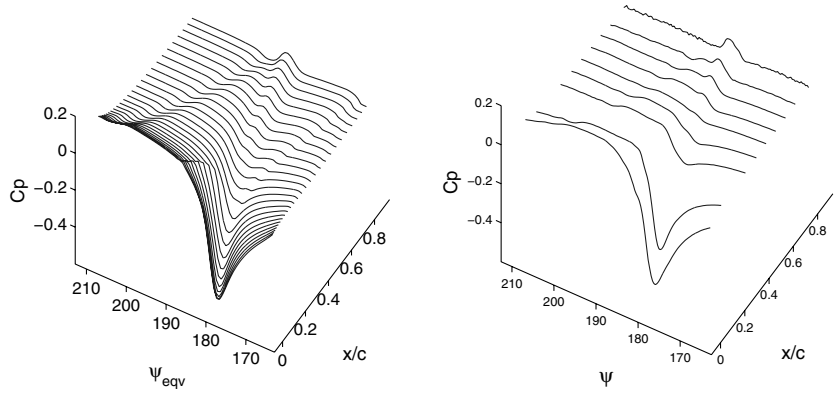

a) CFD on high resolution mesh **b) Experiment**

Fig. 4 Perturbation pressure on lower surface of airfoil for weak two-dimensional AVI, $\frac{Z_v}{c} = 0.25$.

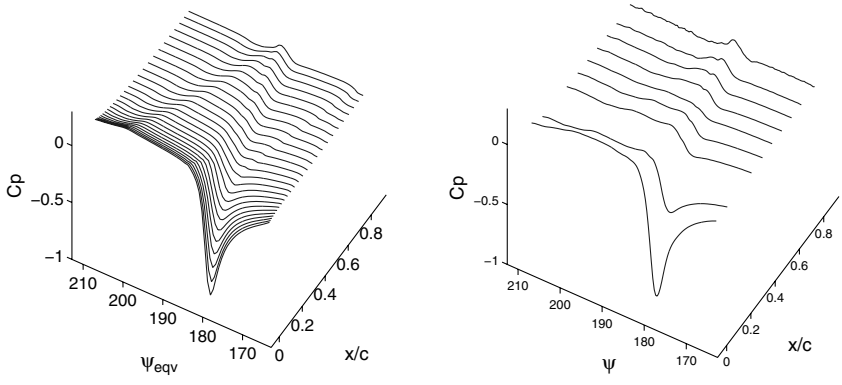

a) CFD on high resolution mesh **b) Experiment**

Fig. 5 Perturbation pressure on lower surface of airfoil for strong two-dimensional AVI, $\frac{Z_v}{c} = 0.0$

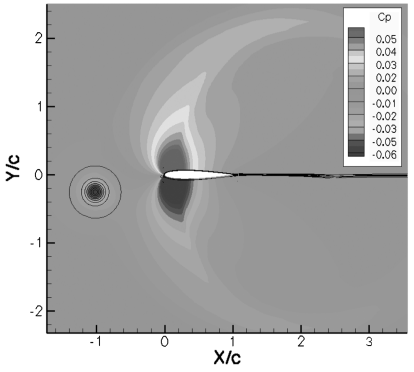

a) Before Interaction. $\psi_{eqv} = 171°$

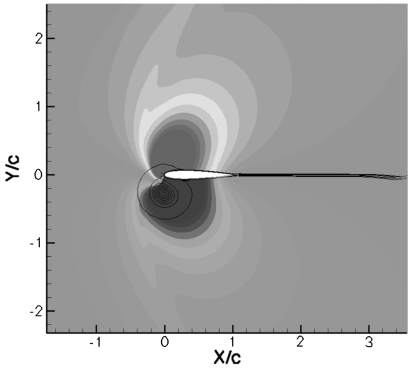

b) Peak pressures position. $\psi_{eqv} = 180°$

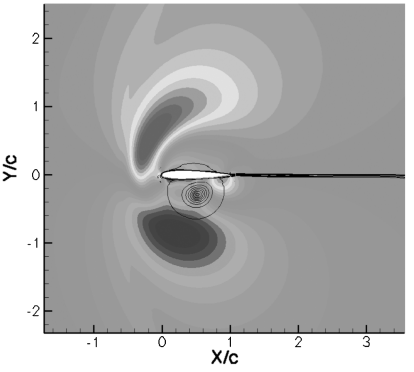

c) Vortex core at midpoint over airfoil. $\psi_{eqv} = 185°$

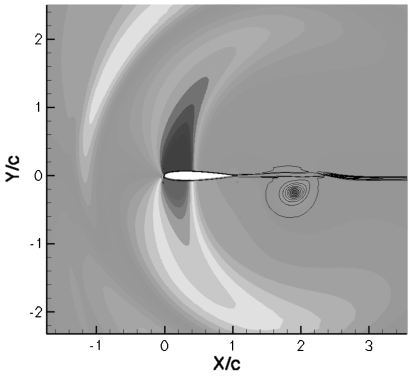

d) Vortex downstream. $\psi_{eqv} = 197°$

Fig. 6 Entropy (contour lines) and perturbation pressure (contour colors) for weak two-dimensional AVI, $\frac{Z_v}{c} = 0.25$.

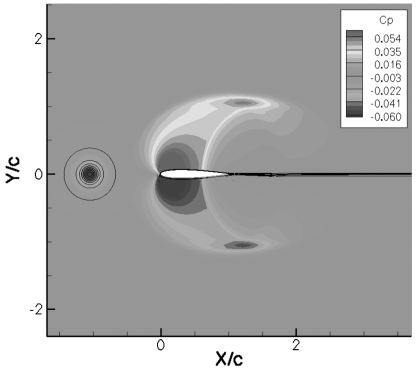

a) Before Interaction. $\psi_{eqv} = 171°$

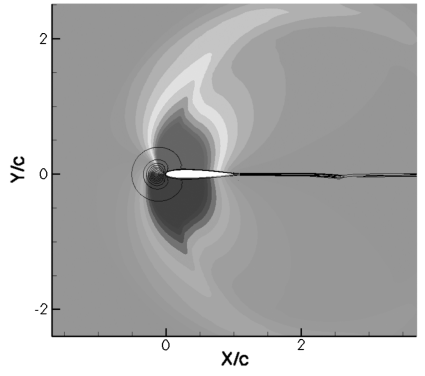

b) Peak pressures position. $\psi_{eqv} = 180°$

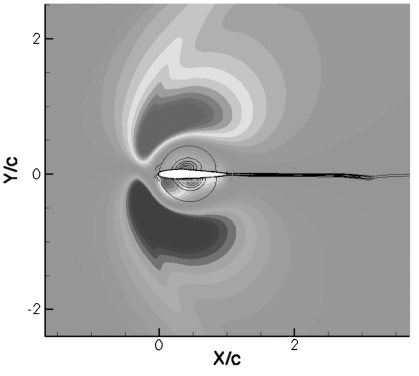

c) Vortex core at midpoint over airfoil. $\psi_{eqv} = 185°$

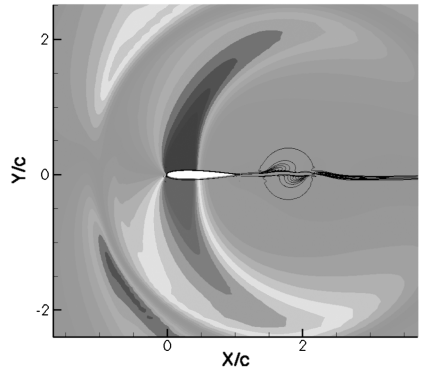

d) Vortex downstream. $\psi_{eqv} = 197°$

Fig. 7 Entropy (contour lines) and perturbation pressure (contour colors) for strong two-dimensional AVI, $\frac{Z_v}{c} = 0$.

For both the weak and the strong interaction cases, the upper surface perturbation pressures have a similar structure but are opposite in sense to that of the lower surface.

The flowfield surrounding the blade during the weak interaction is shown in Fig. 6 and the strong interaction in Fig. 7, both cases share the same fundamental flow features. The lines show contours of entropy, revealing the instantaneous position of the vortex, and the contour colors show the pressure perturbation from the steady value. As the vortex approaches the airfoil (Fig. 6a and 7a), a negative lift is induced. When the vortex is at the leading edge of the airfoil (Fig. 6b and 7b), a peak in perturbation pressure is induced close to the leading edge on the upper surface and an opposite peak is positioned at the corresponding location on the lower surface. As the vortex passes by the leading edge, this peak of the pressure abruptly breaks down and the primary BVI wave is generated. The primary wave can be seen detaching from the airfoil and radiating outward into the surrounding flow (Fig. 6c and 7c) and is the primary acoustic wave, which is negative below the airfoil. At this point, a stable low pressure region is formed on the upper surface as is an opposite high-pressure region on the lower surface. These regions of stable pressure cease to exist when the secondary BVI wave travels upstream from the trailing edge and the secondary acoustic wave is emitted into the flow. This secondary acoustic wave is stronger at the leading edge of the airfoil and produces the distinct far-field acoustic pulse shape. As previously mentioned, the secondary wave is generated as the vortex passes the airfoil trailing edge and is in the opposite pressure sense to the primary wave. The prominent difference between the strong and the weak interactions is the vortex deformation. In the strong interaction the vortex core is bisected and the two sections convect over the airfoil at different speeds due to their individual sense of the edge of the cores with respect to the freestream. These two halves leave the airfoils trailing edge at different times and reform a vortex downstream.

AVI Acoustic Results

The acoustic post processing is performed using the Farassat-1A on-surface formulation of the Ffowcs–Williams and Hawking equations. To calculate the equivalent three-dimensional blade pressures, the two-dimensional AVI results are mapped onto a three-dimensional blade surface and scaled by the local velocity of the rotor blade, which produces a quadratic spanwise variation in pressure towards the blade tip. This method does not include any tip effects but is justified as the experimental rotor is operated at zero thrust. The number of radial stations used in the mapping was varied until the acoustic solution converged. In the present acoustic analysis, 21 radial stations (with clustering towards the blade tip) were used. The near-field microphone is located two chords below the blade and at a span of 88% when the rotor is at 180° azimuth (the azimuthal position where the BVI occurred) and the far-field microphone was approximately 20 chords to the starboard of the rotor hub and 12 chords below the rotor plane. The time histories of the acoustic pressure at the near-field and the far-field microphone are shown in Fig. 8 for the weak interaction and Fig. 9 for the strong interaction.

In general, both the near-field and far-field computed pressures are in good agreement with the experimental data for both the high and low-resolution simulations. The far-field pulse is particularly well resolved in peak value and general pulse shape. The near-field acoustics are dependent on the exact pressure distribution on the airfoil surface and differ from the experimental data slightly.

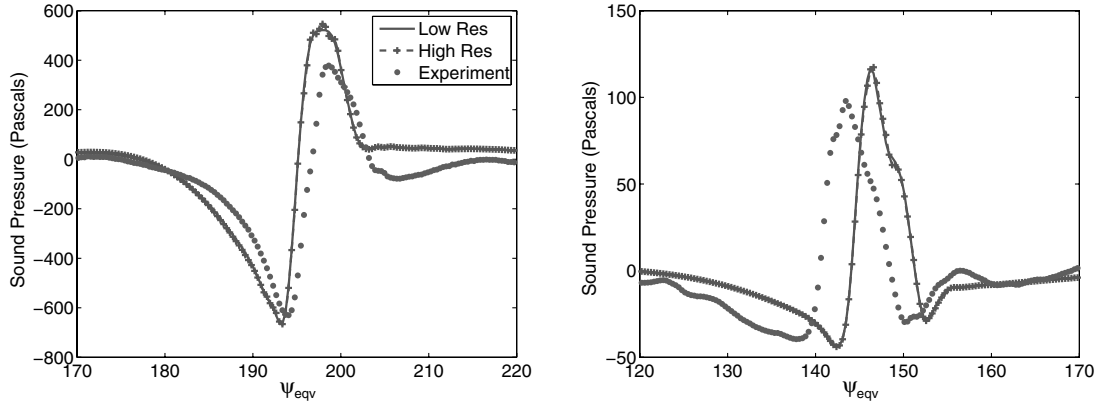

a) Near-field **b) Far-field**

Fig. 8 Acoustic pressure at the near field and the far field for weak two-dimensional AVI, $\frac{z_v}{c} = 0.25$.

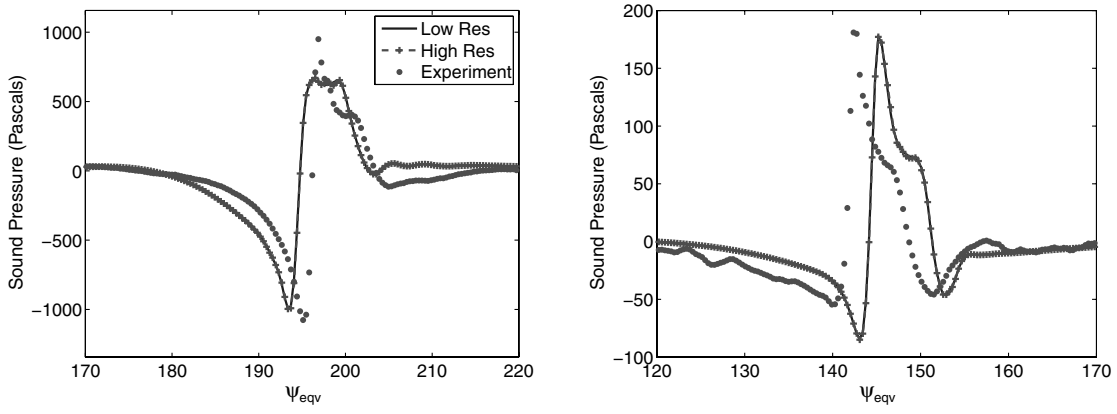

a) Near-field **b) Far-field**

Fig. 9 Acoustic pressure in the near field and far field for strong two-dimensional AVI, $\frac{z_v}{c} = 0.0$.

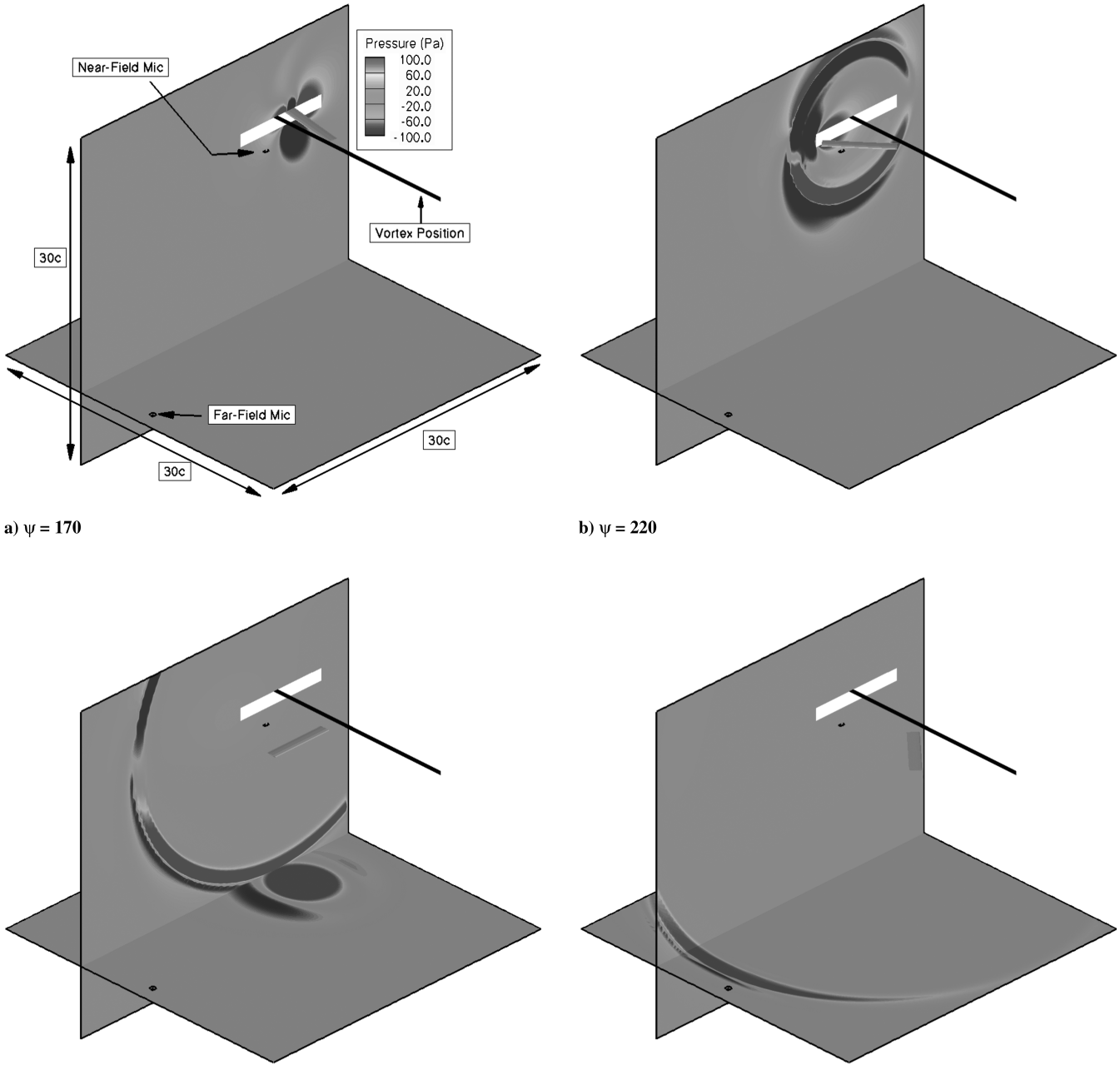

a) ψ = 170 **b) ψ = 220**

c) ψ = 270 **d) ψ = 320**

Fig. 10 Acoustic wave propagation for strong AVI.

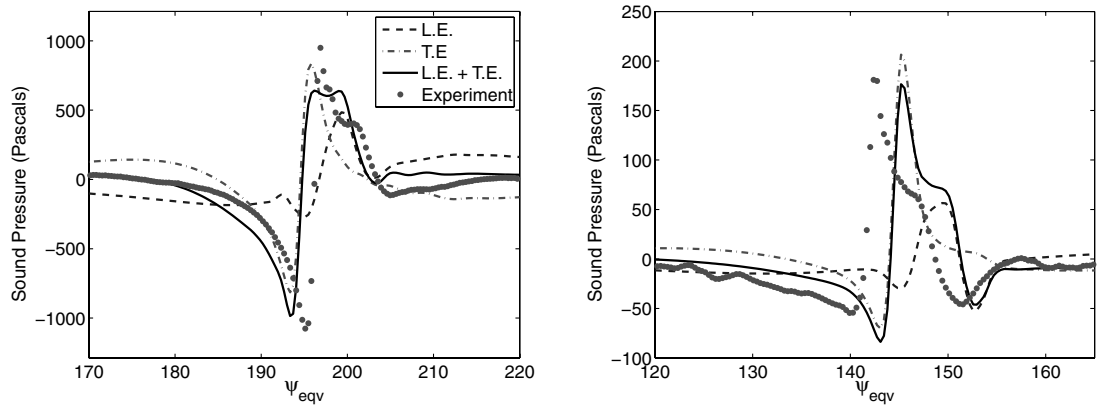

a) Near-field **b) Far-field**

Fig. 11 Acoustic pressure contribution from the leading-edge section (L.E.) and the trailing-edge section (T.E.) of airfoil for a strong AVI.

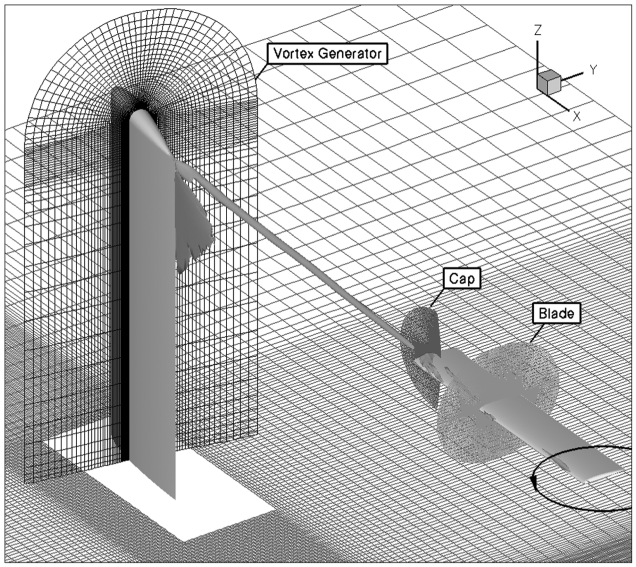

Fig. 12 Overset mesh system for three-dimensional BVI. Vortex position is also shown as surface contour of vorticity.

The acoustic pulses can be broadly understood in terms of the primary and secondary acoustic waves that are emitted from the airfoil surface during the interaction. First, the primary waves are emitted from the airfoil surface which is negative in magnitude below the airfoil. This produces the first negative pulse in the acoustics which is large in the near-field location and less dominant at the far-field location. Following this, the secondary positive acoustic wave is emitted below the airfoil which dominates the acoustics at the far-field location, and is approximately equal and opposite in magnitude to the primary negative pulse at the near-field location. The secondary pulse is stronger than the primary pulse and therefore is the dominant noise in the far field.

This process is illustrated in Fig. 10 which shows the acoustic pressure on two planes as the noise is radiated. The first plane is perpendicular to the airfoil at the time of interaction and is at a location of 88% rotor radius passing through the near-field microphone location. The second plane is parallel to the rotor plane, 2.8 rotor radii below, which coincides with the far-field microphone location. The far-field noise reveals a distinctive kink in the pressure pulse after the peak values. This kink is more prominent in the strong interaction but is also present in the weak interaction. A kink is also present in the near-field acoustics of the strong interaction simulation. It is due to the emission of the secondary acoustic wave from the trailing-edge section of the airfoil. The acoustic waves can be split into contributions from the leading-edge section and the trailing-edge section of the airfoil. The leading-edge section is defined as the portion of the airfoil ahead of the point of maximum thickness and the trailing-edge section as the portion behind. Figure 11 shows the acoustic pressures generated by each of these sections for both the far-field and near-field microphone locations for the strong interaction. The leading-edge airfoil section is seen to radiate the majority of the acoustic energy of both the primary and secondary acoustic pulse. The trailing-edge section contribution is smaller and lags the leading-edge contribution for the microphone positions shown. This lag is due to the microphone locations being ahead of the leading edge at the point of interaction. This lagging of the acoustic waves causes the distinctive kink in the acoustic pulses.

These results show that although the strong and weak interactions are fundamentally different in the way the vortex behaves, the two cases produce qualitatively similar pressure and acoustic results. In the strong interaction, the vortex is severely deformed due to the passage of the airfoil, with the core of the vortex being cut into two separate halves. In the weak interaction, the vortex remains relatively undisturbed by the airfoil passage although a slight change in trajectory was noticed. It should be recognized that this vortex was generated by a wing of chord three times greater than the chord of the airfoil in the interaction. This large vortex generator was required to generate a strong and coherent vortex structure at the freestream wind-tunnel speed. In a realistic rotor the incident vortex, trailed from the preceding blades, can be expected to be much more compact because the core radius is known to scale with the chord of the generating surface. For a more realistic AVI involving a compact vortex, the results are also similar in nature, albeit with some minor differences in detail as shown in Appendix A.

Table 3 Number of cells in three-dimensional BVI meshes

Mesh	Topology	Dimensions	Total points
Vortex generator	C-O	$209 \times 60 \times 51$	639,540
Background	Cartesian	$296 \times 173 \times 135$	6,913,080
Blade	O	$187 \times 157 \times 73$	2,143,207
Cap	——	$111 \times 64 \times 70$	497,280
——	——	——	Sum: 10,058,760

Three-Dimensional BVI

It has been demonstrated that the experiment of Caradonna and Kitaplioglu [7] can be accurately recreated in a two-dimensional AVI simulation thus suggesting that the flow physics relevant to the interaction can be well represented using the current computational method. In this section, additional complexities are introduced in the form of simulating the vortex generation, convection and interaction in three-dimensional. Further, in the two-dimensional AVI simulations, the meshes remain static. In the three-dimensional BVI

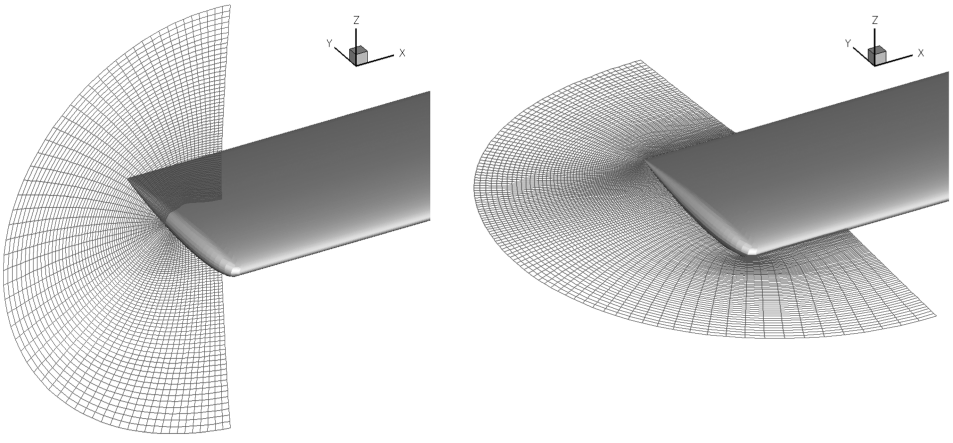

a) b)

Fig. 13 Details of cap mesh topology at rotor blade tip.

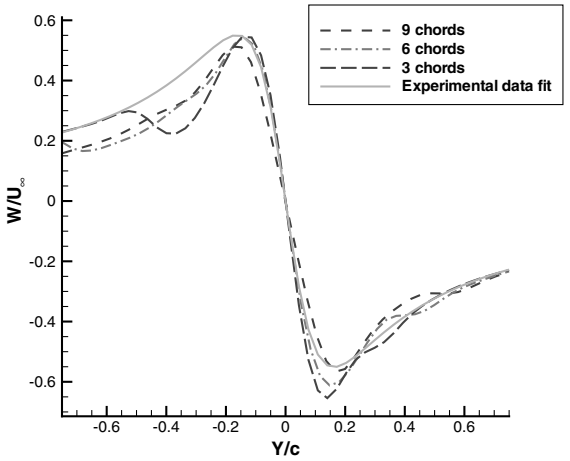

Fig. 14 Velocity profile of experimental fit of vortex and simulated vortex after 3, 6 and 9 chord convection from vortex generator.

simulations, a three-dimensional overset mesh framework is used as shown in Fig. 12, where the meshes are in relative motion to each other. Overset structured grids have the advantage that different grids can be generated independent of each other and can be placed in the region of interest without any distortion. Unlike block structured grids, the grid interfaces need not be matched and this greatly simplifies the grid generation process. This flexibility of grid generation is invaluable in problems like rotorcraft applications, in which surfaces are in relative motion to each other. However, the exchange of data between the meshes increases the complexity.

The mesh dimensions are summarized in Table 3. The vortex generator domain is discretized by a C-O body-conforming grid. A NACA 0015 airfoil section is used and is inclined at an angle of attack of 12° to the freestream, as in the experimental setup. The chord of the vortex generator is three times greater than the rotor blade chord. This mesh is overset onto a Cartesian background mesh. The spacing in the background mesh is refined to 0.035 chords in the areas where the vortex convects, thus creating a high-resolution region where the numerical diffusion can be minimized. The near-blade domain is discretized by two meshes, a C-O topology mesh for the majority of the spanwise length of the blade, and a cap mesh at the tip of the blade. The cap mesh provides a high level of mesh quality at the tip region of the blade where the vortex convects through. The outer boundary of the blade meshes (NACA 0012 airfoil, C-O topology) is at a distance of approximately $0.8c$ from the surface of the airfoil. Details of the cap mesh and its position relative the blade mesh are shown in Fig. 13. The dimensions of these meshes are similar to the preceding low-resolution AVI simulation and are therefore capable of preserving the vortex structure and resolving the salient feature of the interaction.

The simulation is initially performed with all the meshes static until a steady vortex is created by the vortex generator. The profile of this vortex must be of similar strength and structure to the vortex present in the experiment as any variation will have a large change on the strength of the interaction. Figure 14 shows the velocity profile from the simulated vortex and a fit to the experimental data suggested by McAlister and Takahashi [26]. The velocity profile of the simulated vortex is shown at locations of three, six and nine chords downstream of the trailing edge of the vortex generator and it is seen that the profile matches well with the experimental data fit. Note that the vortex will reach the rotor blade after convecting eight chords

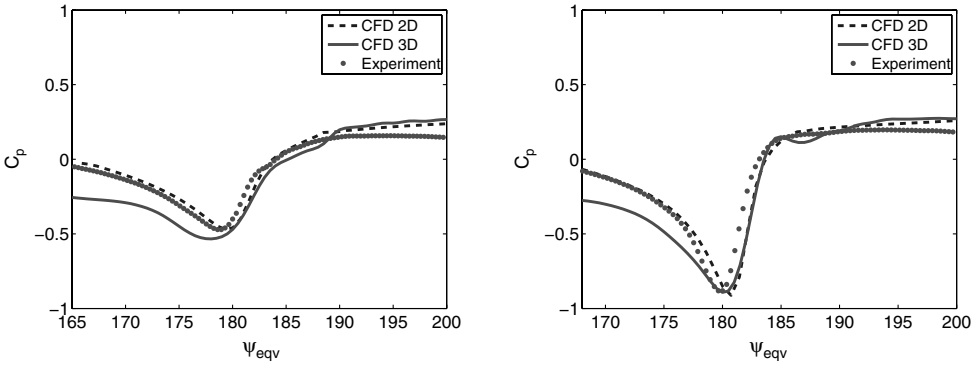

a) Weak BVI **b) Strong BVI**

Fig. 15 Perturbation pressure at $x/c = 0.02$ on the lower surface of the airfoil for weak and strong BVI.

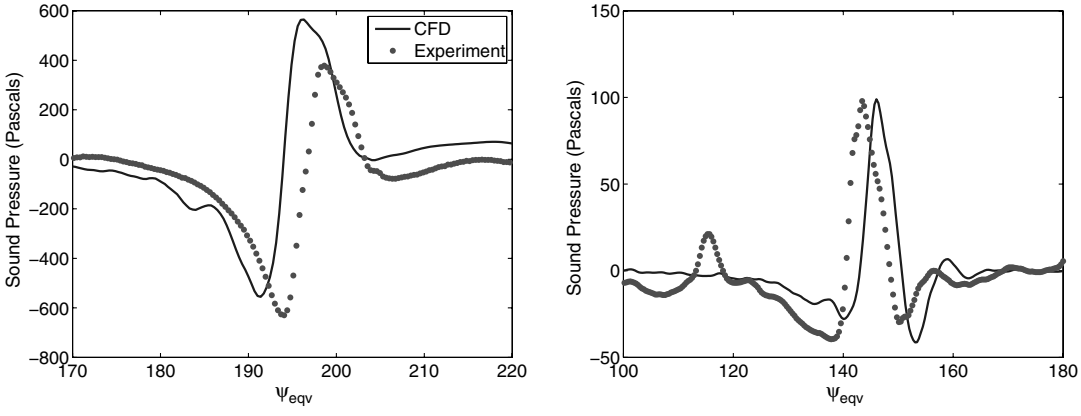

a) Near-field microphone **b) Far-field microphone**

Fig. 16 Acoustic pressure at the far-field and near-field microphone locations for a weak BVI.

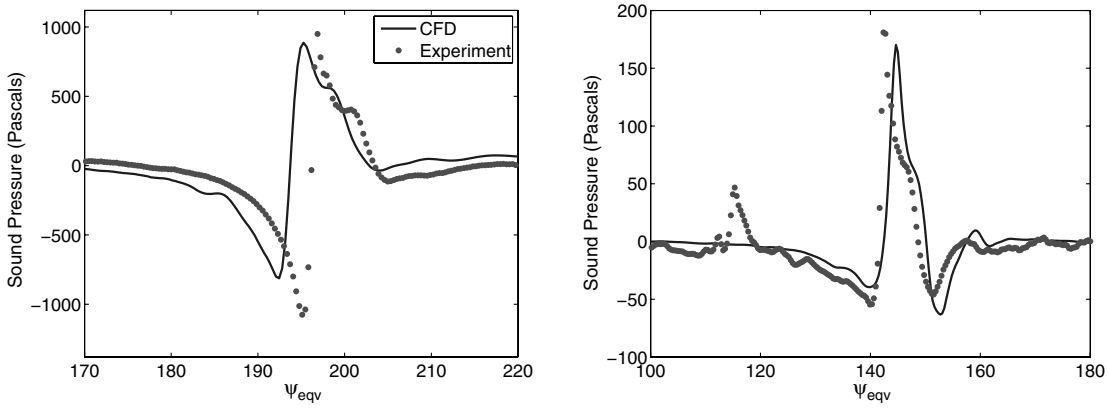

a) Near-field microphone **b) Far-field microphone**

Fig. 17 Acoustic pressure at the far-field and near-field microphone locations for a strong BVI.

downstream of the trailing edge of the vortex generator. At a distance of nine chords downstream of the trailing edge, the profile peak velocity is within approximately 8% of the fitted model value.

Once the steady solution is reached, the rotor blade is rotated at a tip Mach number of 0.715. There are 720 time steps performed per rotor revolution with 15 subiterations per time step and the flow residue was seen to drop over two orders of magnitude every time step. The simulation is performed using a second order backward in time scheme to solve the time integration as this has been shown to better preserve the strength of the vortex as it is passes across mesh interfaces [28]. The solution is run for three revolutions with data being collected on the last revolution.

Similar to the AVI analysis, two simulations are presented here, a weak interaction where the blade misses the vortex by a quarter chord and a strong interaction where the vortex impact directly on the blade.

BVI Surface Pressure Results

The computed perturbation pressures on the blade surface from the simulation of the weak interaction are shown in Fig. 15a, at a location of $x/c = 0.02$ on the lower surface against the experiments of Caradonna and Kitaplioglu [7]. The two-dimensional AVI results have also been shown for comparison. Both the magnitude and phase of the pressure pulses have been captured in these simulations. In particular the gradient of the pressure pulse after the point of maximum absolute pressure matches well with experimental data. This pressure gradient is important for the acoustic analysis and is directly related to the magnitude of the sound pulse generated by the interaction.

The computed perturbation pressures on the blade surface from the simulation of the strong interaction are shown in Fig. 15b, at a location of $x/c = 0.02$ on the lower surface. In this case, severe vortex deformation occurs. Again, both the magnitude and phase of these pressure pulses have been captured well in these simulations indicating that the effect of the deformation of the vortex is being resolved. The gradient of the pressure pulse is also in good agreement with the experimental data. The three-dimensional CFD results and the experimental data differ in pressure values before and after the interaction. This is most likely caused by differences between the experimental and resolved vortex in the CFD simulation inducing different surface pressures on the airfoil.

BVI Acoustic Results

The acoustic pressures computed for the weak interaction case are shown in Fig. 16 and the strong interaction is shown in Fig. 17. In general, the near-field pressure pulse has been calculated well but differs for the experimental data in peak value. It has been show previously that this acoustic analysis is capable of reproducing the near-field acoustics accurately if the surface pressures are well resolved [29]. This is an indication that near-field acoustics are quite sensitive to the surface pressures. In addition, this analysis neglects any quadrupole noise sources which have a more prominent influence in the near-field acoustics.

The peak magnitude of the computed pressure pulse at the far-field microphone is in good agreement with the experimental value for both the strong and weak interaction simulations. A phase difference is evident in the acoustic pressures for both simulations. This is thought to result, in part, from the vortex position being shifted as it is interpolated into the blade mesh as noted in the previous studies [28]. It should be noted that uncertainties exist about the exact location of the vortex relative to the blade in the experimental study due to vortex wandering. It should also be noted that the distinctive kink produced by the pressure radiated from the trailing edge of the airfoil is present in these calculations.

Conclusions

High-resolution simulations of parallel BVIs were performed using the solution of the compressible Euler equations on overset meshes and representative pressure and acoustic results were compared with the experiments of Caradonna and Kitaplioglu [7]. This study has focused on both a weak interaction where the vortex passes below the blade by a quarter chord, and a strong interaction where the blade impact directly upon the vortex. The acoustic pressures are calculated from a solution of the Farassat-1A on-surface formulation of the Ffowcs–Williams and Hawking equations. Both two and three-dimensional analysis are performed.

The initial simulations resolved a two-dimensional AVI on a static overset mesh system. In this approach, the vortex is initialized as a perturbation to the flow and is allowed to freely convect and interact with the airfoil. During the strong interaction, the vortex is observed to split into two halves that convect above and below the airfoil surface at varying speeds. Good agreement between the computed surface pressures and the measured data was demonstrated and the experimentally observed primary and secondary surface BVI waves were shown to be captured to a high degree of accuracy. The near-field acoustic pressures are observed to be influenced equally by the primary and secondary acoustic waves whereas the far-field microphone noise appears to be more heavily influenced by the secondary acoustic waves.

To extend the simulation to three dimensions, a computational framework of moving overset meshes was used. The simulation is performed with an attempt at resolving the generation of a vortex from a fixed wing, its convection and interaction with the rotor blade akin to the experiments of Caradonna and Kitaplioglu [7]. The vortex was seen to accurately match the experimental vortex velocity profile and convect through the solution without significant diffusion. The blade surface pressure results from the BVI were shown to agree well with the experimental measurements. The computed near and far-field acoustic pressure time histories show

excellent agreement with experiment in terms of pulse shape and amplitude. The range of simulations presented in this paper confirm the ability of the methodology to accurately model the aerodynamics and acoustics of a direct impact BVI. Particularly, the deformation of the vortex as it interacts with the blade is well captured and is an improvement over previous studies where the vortex was imposed as a constant strength perturbation. The flexibility of moving overset mesh framework mean that the present calculations can be easily extended to practical helicopter configurations given adequate computational resources.

Appendix A: AVI Involving a Compact Vortex

A two-dimensional AVI simulation with a compact vortex (core radius of $0.075c$) is performed to ascertain the extent to which this interaction differs from the two-dimensional AVI simulation presented in the paper (which involved a core radius of $0.162c$). The mesh and freestream velocity are kept the same as the previous two-dimensional AVI simulations. Figure A1a shows the perturbation surface pressure on the lower surface of the airfoil during a strong interaction involving a compact vortex. The peak magnitude of the pressure is greater than the previously simulated case involving the larger vortex (Fig. 3b). This is to be expected as the more compact vortex will induce stronger gradients. The basic mechanism of the pressure waves is the same for the previous case and the interaction follows a similar sequence. However, subtle differences in the details of the surface pressure are observed in the downstream half of the airfoil. Figure A1b shows the trailing-edge section of the airfoil during the strong AVI with the compact vortex and Fig. A1c shows the trailing-edge section of the strong AVI with the normal vortex for comparison. The compact vortex pressure surface reveals a distinct ridge of pressure that occurs close to the peak of the primary BVI wave. This is a result of the stronger vortex core traveling along the airfoil surface. A similar event can be seen in the normal vortex AVI but much weaker due to the weaker vortex core.

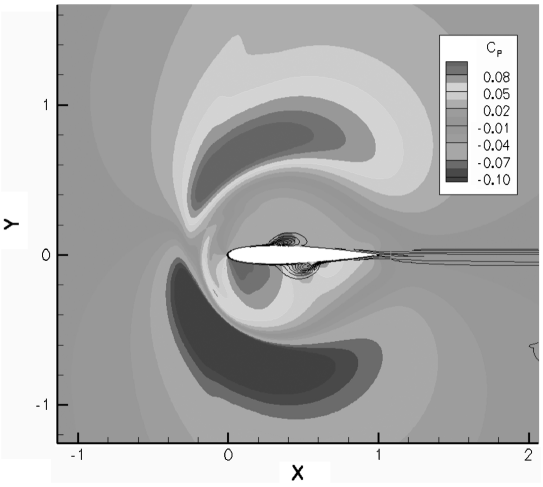

Fig. A2 Flow solution as compact vortex interacts with airfoil. Contour colors represent pressure, contour lines represent vorticity.

A snapshot of the flowfield is shown in Fig. A2 at an instant when the vortex has convected approximately half the chord across the airfoil surface. Similar to the previous simulations, the airfoil cuts the vortex core and the vortex is severely distorted. The compact vortex case differs from the previous simulation in that a larger portion of the core is seen to convect along the lower side of the airfoil. The signature of this core is seen as a ridge in Fig. A1b.

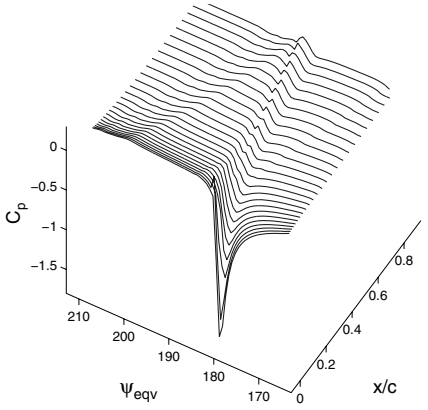

a) C_p on lower surface of airfoil for compact vortex AVI

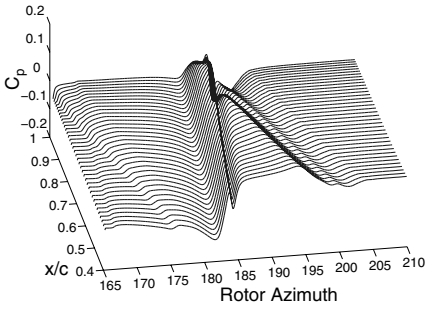

b) C_p on lower surface of airfoil for compact vortex AVI

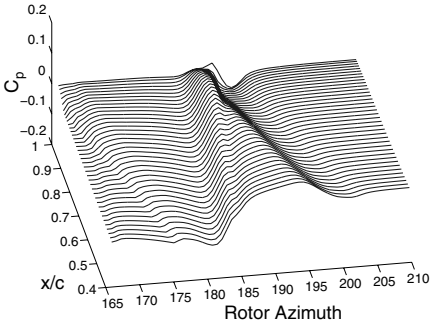

c) Cp on lower surface of airfoil for normal vortex AVI (downstream half of airfoil)

Fig. A1 Surface of C_p lower surface of airfoil for two-dimensional AVI.

Acknowledgments

The authors would like to thank Cahit Kitaplioglu for providing the experimental data and Jay Sitaraman for his assistance with the acoustic modeling.

References

[1] JanakiRam, R., "Aeroacoustics of Rotorcraft," AGARD Fluid Dynamics Panel Special Course, 1990.

[2] Kube, R., Splettstoesser, W. R., Wagner, W., Seelhorst, U., Yu, Y. H., Tung, C., Beaumier, P. J., Prieur, G. Rahier, P. S., Boutier, A., Brooks, T. F., Burley, C. L., Boyd, D. D., Mercker, E., and Pengel, K., "HHC Aeroacoustic Rotor Tests in the German–Dutch Wind Tunnel: Improving Physical Understanding and Prediction Codes," *Aerospace Science and Technology*, Vol. 2, No. 3, 1998, pp. 177–190. doi:10.1016/S1270-9638(98)80052-7

[3] van der Wall, B., Junker, B., Burley, C., Brooks, T., Yu, Y., Tung, C., Raffel, M., Richard, H., Wagner, W., Mercker, E., Pengel, K., Holthusen, H., Beaumier, P., and Delrieux, Y., "The HART 2 Test in the LLF of the DNW: A Major Step Towards Rotor Wake Understanding," *Proceedings of the 28th European Rotorcraft Forum*, Bristol, England, 2002.

[4] Lim, J., Nygaard, T., Strawn, R., and Potsdam, M., "BVI Airloads Prediction Using CFD/CSD Loose Coupling," AHS Vertical Lift Aircraft Design Conference, San Francisco, CA, 2006.

[5] Duraisamy, K., and Baeder, J., "High Resolution Wake Capturing Methodology for Hovering Rotors," *Journal of the American Helicopter Society*, Vol. 52, No. 2, 2007.

[6] Wake, B. E., and Choi, D., "Investigation of High-Order Upwinded Differencing for Vortex Convection," *AIAA Journal*, Vol. 34, No. 2, 1996, pp. 332–337. doi:10.2514/3.13068

[7] Caradonna, F., and Kitaplioglu, C., "A Study of Blade–Vortex Interaction Aeroacoustics Utilizing an Independently Generated Vortex," AGARD Fluid Dynamics Panel Symposium on Aerodynamics and Aeroacoustics of Rotorcraft, Berlin, Germany, 10–14 Oct. 1994.

[8] Horner, M. B., Saliveros, E., Kokkalis, A., and Galbraith, R. A. M., "Results from a Set of Low Speed Blade–Vortex Interaction Experiments," *Experiments in Fluids*, Vol. 14, No. 5, 1993, pp. 341–352.

[9] Oh, W. S., Kim, J., and Kwon, O. J., "Numerical Simulation of Two-Dimensional Blade–Vortex Interactions Using Unstructured Adaptive Meshes," *AIAA Journal*, Vol. 40, No. 3, 2002, pp. 474–480. doi:10.2514/2.1670

[10] Morvant, R., Badcock, K., Barakos, G., and Richards, B., "Airfoil–Vortex Interaction Using the Compressible Vorticity Confinement Method," *AIAA Journal*, Vol. 43, No. 1, Jan. 2005.

[11] Ilie, M., "Numerical Study of Helicopter Blade–Vortex Mechanism of Interaction Using Large-Eddy Simulation," *Computers and Structures*, Vol. 87, Nos. 11–12, 2009, pp. 758–768.

[12] Leishman, J., "Aeroacoustics of Two-Dimensional and Three-Dimensional Blade Vortex Interaction Using the Indicial Method," American Helicopter Society 52nd Annual Forum, Washington, D. C., 4–6 June 1996.

[13] Bridgeman, J. O., Ramachandran, K., Caradonna, F. X., and Prichard, D. S., "A Computational Analysis of Parallel Blade–Vortex Interactions Using Vorticity Embedding," American Helicopter Society 50th Annual Forum Proceedings, Washington, D. C, May 1994.

[14] Srinivasan, G. R., and Baeder, J. D., "Flowfield of a Lifting Rotor in Hover: A Navier–Stokes Simulation," *AIAA Journal*, Vol. 30, No. 10, 1992, pp. 2371–2378. doi:10.2514/3.11236

[15] McCluer, M., "Helicopter Blade–Vortex Interaction Noise with Comparisons to CFD Calculations," NASA Ames Research Center, TM 110423, Moffett Field, CA, Dec. 1996.

[16] Strawn, R. C., Oliker, L., and Biswas, R., "New Computational Methods for the Prediction and Analysis of Helicopter Acoustics," *Journal of Aircraft*, Vol. 34, No. 5, 1997, pp. 665–672. doi:10.2514/2.2227

[17] Thom, A., and Duraisamy, K., "High Resolution Computation of the Aerodynamics and Acoustics of Blade Vortex Interaction," 34th European Rotorcraft Forum, Liverpool, England, Sept. 2008.

[18] Duraisamy, K., and Brown, R., "Aerodynamic Response of a Hovering Rotor to Ramp Changes in Pitch Input," *Proceedings of the American Helicopter Society 64th Annual Forum*, Montreal, Canada, 2008.

[19] Cockburn, B., Johnson, C., Shu, C., and Tadmor, E., "Essentially Non-Oscillatory and Weighted Essentially Non-Oscillatory Schemes for Hyperbolic Conservation Laws," *Lecture Notes in Mathematics*, Vol. 1697, 1998, pp. 325–432.

[20] Rumsey, C., Sanetrik, M., Biedron, R., Melson, N., and Parlette, E., "Efficiency And Accuracy of Time-Accurate Turbulent Navier–Stokes Computations," 13th AIAA Applied Aerodynamics Conference, 19–22 June 1995.

[21] Brentner, K., and Farassat, F., "Modeling Aerodynamically Generated Sound of Helicopter Rotors," *Progress in Aerospace Sciences*, Vol. 39, 2003.

[22] Gopalan, G., Sitaraman, J., Baeder, J., and Schmitz, F., "Aerodynamic and Aeroacoustic Prediction Methodologies with Applications to the HART-2 Model Rotor," 62nd Annual Forum of the American Helicopter Society, 9–11 May 2006.

[23] Caradonna, F., Kitaplioglu, C., and McCluer, M., "Methods for the Prediction of Blade–Vortex Interaction Noise," American Helicopter Society Technical Specialists' Meeting for Rotorcraft Acoustics and Aerodynamics, Williamsburg, VA, Oct. 1997.

[24] Caradonna, F. X., Kitaplioglu, C., and McCluer, M., "An Experimental Study of Parallel Blade–Vortex Interaction Aerodynamics and Acoustics Utilizing an Independently Generated Vortex," NASA Ames Research Center, TM 199208790, Moffett Field, CA, July 1999.

[25] Duraisamy, K., "Studies in Tip Vortex Formation, Evolution and Control," Ph.D. Thesis, Department of Aerospace Engineering, University of Maryland, College Park, MD, Feb. 2005.

[26] McAlister, K. W., and Takahashi, R. K., "NACA 0015 Wing Pressure and Trailing Vortex Measurements," NASA Ames Research Center, TP 3151, Moffett Field, CA, Nov. 1991.

[27] Tanabe, Y., Saito, S., Takasaki, K., and Fujita, H., "A Parametric Study on Parallel Blade–Vortex Interaction for Helicopter Rotor," Japan Aerospace Exploration Agency Rept. JAXA-RR-07-051E, Feb. 2008.

[28] Thom, A., and Duraisamy, K., "Numerical Investigation of the Aerodynamics and Acoustics of Head-On Blade–Vortex Interaction," 65th American Helicopter Society Annual Forum, Grapevine, TX, May 2009.

[29] Kitaplioglu, C., Caradonna, F. X., and Burley, C. L., "Parallel Blade–Vortex Interactions: An Experimental Study and Comparison with Computations," American Helicopter Society Second International Aeromechanics Specialists' Conference, 11–13 Oct. 1995.

C. Bailly
Associate Editor